Facile and secure synthesis of porous partially fluorinated graphene employing weakly coordinating anion for enhanced high-performance symmetric supercapacitor

Ning Cao, Teng Wang, Rabah Boukherroub, Yinghui Cai, Yijiang Qin, Fashun Li, Peng Liu, Qingguo Shao, Mingle Liu, Xiaobei Zang

Journal of Materiomics 8 (2022) 113–122

Contents lists available at ScienceDirect

Journal of Materiomics

journal homepage: www.journals.elsevier.com/journal-of-materiomics/

Facile and secure synthesis of porous partially fluorinated graphene employing weakly coordinating anion for enhanced high-performance symmetric supercapacitor

Ning Cao [a], Teng Wang [a], Rabah Boukherroub [b], Yinghui Cai [c], Yijiang Qin [a], Fashun Li [a], Peng Liu [a], Qingguo Shao [a], Mingle Liu [d], Xiaobei Zang [a, *]

[a] School of Materials Science and Engineering, China University of Petroleum (East China), Qingdao, 266580, China
[b] Univ. Lille, CNRS, Centrale Lille, Univ. Polytechnique Hauts-de-France, UMR 8520 - IEMN, F-59000, Lille, France
[c] Chambroad Holding Group, Economic Development Zone, Binzhou, 256500, China
[d] China Petroleum Pipeline Engineering Co., Ltd, Asia Pacific Branch, China Petroleum Pipeline Engineering Co., Ltd., Development Zone, Langfang, 065000, China

ARTICLE INFO

Article history:
Received 25 March 2021
Received in revised form
24 April 2021
Accepted 28 April 2021
Available online 18 May 2021

Keywords:
Partially fluorinated graphene
Weakly coordinating anion
Semi-ionic C
F bonds
Supercapacitors

ABSTRACT

In this paper, porous partially fluorinated graphene (PFG) for supercapacitors (SCs) was fabricated by a mild and secure one-pot hydrothermal method utilizing weakly coordinating anion BF_4^- as the fluorine source. The hydrolysis rate of sodium fluoroborate was adjusted by controlling the reaction temperature and PFG containing semi-ionic C–F bonds was obtained, where the content of semi-ionic C–F bonds in PFG can be easily regulated. The final experimental results show that the incorporation of fluorine not only modulates the electrochemical properties of the material, but also creates abundant pores. When assembled in a symmetric supercapacitor, the PFG shows a high specific capacitance of 269.7 F g^{-1} at 1 A g^{-1} and a superior rate capability with 89.3% capacitance retained, as the current density is increased from 1 A g^{-1} even to 20 A g^{-1}. Furthermore, the resultant energy density for PFG is 9.4 Wh kg^{-1} at a power density of 250.0 W kg^{-1} (1 A g^{-1}). All these results confirm that as-prepared partially fluorinated graphene is appropriate for the application in SCs and mass production.

1. Introduction

The depletion of fossil fuel and the devastation of the ecological environment accelerate reform of the energy transition [1–4]. The recent years have witnessed the increasing tendency of gradual conversion from fuel vehicles to electric vehicles. Besides, electronic equipment such as smartphones is constantly upgrading with higher requirements for energy storage components. Among the diverse electrochemical storage devices, supercapacitors (SCs), which are different from rechargeable batteries with relatively high energy density, will also have wide prospects in future marketplaces due to the features of higher power density, longer cyclic life and better safety [5–8]. According to the energy storage mechanism, SCs can be divided into electric double-layer capacitors (EDLC) and pseudo-capacitors [9]. The choice of electrode materials is a critical factor affecting their electrochemical performances. Carbon materials, as typical electrode materials of EDLC, possess numerous advantages such as good electrical conductivity and outstanding power density [10]. And at the foreground of carbon materials, graphene has been a desired candidate for SCs application since it has a high specific surface area (2630 m^2 g^{-1}), good electronic conductivity and high electrochemical stability [11–13].

Considering that pristine carbon materials apparently cannot satisfy the actual demands for SCs, functionalization is deemed an effective strategy to improve their basic properties. In recent years, the introduction of heteroatoms like nitrogen (N), sulfur (S), phosphorus (P) atoms into carbon materials to achieve functionalization has become a hot topic. Abundant previous works on fluorinated/fluorine-doped carbon-based electrode materials for SCs have validated that the introduction of fluorine element into carbon materials is beneficial to the electrochemical performance improvement of SCs. Zhou *et al.* [14] synthesized fluorine and nitrogen co-doped non-porous carbon microsphere by low-

* Corresponding author.
E-mail address: xiaobeizang@upc.edu.cn (X. Zang).
Peer review under responsibility of The Chinese Ceramic Society.

https://doi.org/10.1016/j.jmat.2021.04.012

temperature solvothermal method. Ultrahigh volumetric capacitance of 521 F cm^{-3} and cycling stability with no capacitance loss even after 10 000 cycles at 5 A g^{-1} were obtained in aqueous electrolyte. This study pointed out that the incorporation of fluorine could dramatically enhance volumetric capacitance. Zhou *et al.* [15] fabricated fluorine-rich nano-porous carbons (FNC), which were firstly activated by KOH to enlarge the pore size and next washed with hydrofluoric acid and nitric acid. The assembled symmetric cell in organic electrolyte exhibited a high specific capacitance of 168 F g^{-1} at 0.5 A g^{-1} and a capacitance retention of 92% after 10 000 cycles. An *et al.* [16] synthesized fluorinated graphene hydrogel via single-step hydrothermal process with HF as a fluorinating agent. The capacitance of symmetric supercapacitor achieved 180 F g^{-1} at 1 A g^{-1}, and the corresponding energy density and power density were respectively 5.55 Wh kg^{-1} and 505.8 W kg^{-1}. Due to the existence of various sorts of C–F bonds, especially semi-ionic C–F bonds, the conductivity and wettability for electrolyte of materials was vastly ameliorated [17,18].

It is worth noting that the electronic properties of fully fluorinated graphene have been well revealed owing to its stable structure as well as relevant experimental and computational studies [19]. However, the complex nature and difference levels of fluorination allows partially fluorinated graphene to exhibit variable electronic performances. The electrochemical performances of them are mainly determined by the preparation method, the level of fluorine coverage, fluorinating agent and so on. On the one hand, as we all known, the reason why single-layer graphene possesses high electron mobility is actually due to its sp^2 hybridized C atoms with a p_z orbital. In covalent C–F bonds, C atoms are present in the form of sp^3-hybridization. However, C atoms in semi-ionic C–F bonds still exist in the form of sp^2-hybridization. Hence, it is expected that semi-ionic C–F bonds dominate competing reaction processes between these two main types of C–F bonds. Deeply tapping the potential of partially fluorinated graphene for SCs is also endowed with great significate in the future.

On the other hand, the common methods of preparing fluorinated graphene include gas-phase fluorination (F_2, XeF_4), hydrothermal fluorination (HF, NH_4F, Diethylaminosulphur trifluoride (DAST)), plasma fluorination (SF_6, CF_4) and so on [20–26]. Although these gaseous or liquid fluorinating agents aforementioned have strong fluorinating ability, they could make operators exposed to potential danger (extremely strong corrosivity) or have high demand to the apparatus for experiment and mass production. Herein, the secure, facile and cost-effective synthesis of partially fluorinated graphene will become one of major research orientation simultaneously solving the problems of mass production. Meanwhile, because the semi-ionic C–F bond tends to present at low fluorine concentration, it is also a challenge that creating an appropriate reaction environment to form semi-ionic C–F bonds for graphene oxide [27]. This semi-ionic C–F bond, in which F acts as p-dopant for graphene, has long been recognized as the main contributor on the improvement of electrochemical performances [28,29]. Therefore, researchers are expected to make further efforts to explore the moderate preparation method of partially fluorinated graphene and its relevant reaction mechanism.

In order to address the above problems, we put forward a facile and secure one-pot hydrothermal method to fabricate porous partially fluorinated graphene using $NaBF_4$ as the mild fluorinating agent. In different types of C–F bonds, almost only semi-ionic C–F bonds are obtained in partially fluorinated graphene prepared at 180 °C, thus achieving the optimum performance for supercapacitors. Different from traditional hydrothermal direct fluorination which utilizes HF, NH_4F or $(C_2H_5)_3N{\cdot}3HF$, etc. to achieve large accumulation of fluoride ions at first, the two-step reaction process can keep fluorination of GO at low fluorine concentration. Specifically, during the preparation process of partially fluorinated graphene, there actually need these two steps including: (1) hydrolysis process of weakly coordinating anion BF_4^- to produce a few HF, (2) nucleophilic substitution between GO and HF to synthesize partially fluorinated graphene. Consumption of F^- in step (2) promoted continuous hydrolysis of BF_4^- of the step (1). Since the hydrolysis reaction is an endothermic reaction, the hydrothermal temperature is the chief factor affecting the degree of fluorination of GO. In order to obtain a good partially fluorinated graphene electrode material with optimum electrochemical performance, we varied the reaction temperature during fluorination. As-fabricated 180-PFG showed excellent super-capacitive behavior of 281.4 F g^{-1} at 1 A g^{-1} in three-electrode system. Assembled symmetric supercapacitors similarly possessed a splendid specific capacitance of 269.7 F g^{-1} at 1 A g^{-1}. Notably, it also had an extremely high retention of 89.3% even at 20 A g^{-1}. Such a green and secure synthesis for partially fluorinated graphene is suitable for large-scale production due to the advantages of convenient storage and transportation of this fluorinating agent.

2. Experimental section

2.1. Materials

Sodium fluoroborate ($NaBF_4$, ≥99.0%) was purchased from Shanghai McLean Biochemical Technology Co., Ltd. (Shanghai, China). Graphene oxide (GO) synthesized by modified Hummers' method was bought from Nanjing XFNANO materials Tech. Co. Ltd. (Nanjing, China). Potassium hydroxide (KOH, ≥ 85.0%) was obtained from Sinopharm Group Co., Ltd. (Shanghai, China). Ni foam (purity ≥ 98%, thickness 0.5 mm) was purchased from Shanxi Lizhiyuan Battery Material Co., Ltd. (Taiyuan, China). N-methyl-2-pyrrolidone (NMP), acetylene black (battery grade) and polyvinylidene fluoride (PVDF) were bought from Shenzhen Teensky Technology Co. Ltd. (Shenzhen, China). All the received chemical agents were used without further purification. Deionized (DI) water was gained from the laboratory.

2.2. Fabrication of partially fluorinated graphene (PFG) and hydrothermally reduced graphene oxide (HRG)

The 40 mg GO sheets were dissolved in 60 ml DI water by ultrasonication for 1 h until there were no visible particulates. Then, 1.2 g sodium fluoroborate ($NaBF_4$) was added into the PTFE griffin beaker. The mixture was continuously ultra-sonicated for another 30 min, then transferred into 100 ml Teflon-lined autoclave at the specific temperature (120 °C, 140 °C, 160 °C, 180 °C and 200 °C) for 24 h. For comparison, the same hydrothermal process was conducted at 180 °C for graphene oxide solution only without adding $NaBF_4$ powder. Then, partially fluorinated graphene (PFG) and hydrothermally partially reduced graphene oxide (HRG) were rinsed with deionized water and filtrated for several times. Finally, these samples were obtained by freeze drying for 24 h to remove residual moisture. PFGs prepared under various temperatures were labeled as x-FPG (x represents reaction temperature).

2.3. Characterization

The morphology and microstructure of samples were investigated by field-emission scanning electron microscopy (FESEM, JEOL JSM-72F) and transmission electron microscopy (TEM, FEI Titan G260-300). X-ray diffraction (XRD) patterns were recorded on a D8 Advance (Bruker) X-ray diffractometer with Cu Kα radiation. X-ray photoelectron spectroscopy (XPS) measurements were made using a PHI Quantum 2000 Scanning ESCA Microprobe (Eden Prairie, MN,

USA). Raman spectrum measurements were conducted in a HR Evolution with a 532 nm excitation laser. Fourier transform infrared (FT-IR) spectroscopy were recorded on a Nicolet 6700 (Thermo-Fisher, Waltham, MA, USA). The nitrogen adsorption-desorption isotherm was measured using Brunauer-Emmett-Teller (BET) theory by micromeritics ASAP2460 (USA).

2.4. Electrochemical measurements

The electrochemical properties of the as-prepared samples were carried out on a Solartron Modulab XM electrochemical workstation and LAND battery measurement system (CT3001K). All electrochemical tests were performed in 6 M KOH electrolyte. In the three-electrode system, active materials, acetylene black and polyvinylidene fluoride (PVDF) binder in a mass ratio of 80:10:10 were dispersed in N-methyl-2-pyrrolidone (NMP) by stirring to form the homogeneous slurry. The working electrodes were fabricated by pasting slurry on a 1 × 1 cm^2 nickel foam as the current collector, and then dried at 100 °C overnight in vacuum. Platinum plate and saturated calomel electrode (SCE) were selected as the counter electrode and reference electrode, respectively. The mass of the active material on the Ni foam was controlled close to 2.5 mg cm^{-2}. Cyclic voltammetry (CV) and galvanostatic charge-discharge (GCD) curves were measured with potential ranging from −1.2 V to −0.2 V (vs. SCE). Electrochemical impedance spectroscopy (EIS) tests were measured in the frequency range from 0.01 Hz to 10^5 Hz with a potential amplitude of 10.0 mV.

Coin-type symmetric supercapacitor device (CR2032) was assembled with Ni foam of 12 mm in diameter coated with the slurry by a brush and a cellulose membrane separator. Cyclic voltammetry (CV) curves at various scan rates from 5 mV s^{-1} to 200 mV s^{-1} were performed over a potential range of 0–1.0 V. Galvanostatic charge-discharge (GCD) curves were measured in the same potential window as CV tests. Only the cyclic stability tests of devices were measured on the CT3001K at 4 A g^{-1}. The mass specific capacitance (C_s, F g^{-1}) of single electrode material was calculated according to equitation (1). The specific capacitance (C_d, F g^{-1}), energy density (E, Wh kg^{-1}) and power density (P, W Kg^{-1}) were obtained according to equations (2)–(4), respectively [30,31].

$$C_s = \frac{2I\Delta t}{m\Delta V} \tag{1}$$

$$C_d = \frac{1}{4}C_s \tag{2}$$

$$\mathrm{E} = \frac{\frac{1}{2}C_d\Delta V^2}{3.6} \tag{3}$$

$$P = \frac{3600E}{\Delta t} \tag{4}$$

where I represents the constant current (A), m represents the mass of single electrode material (g), ΔV represents the operation potential window (V), and Δt represents the discharge time (s).

3. Results and discussion

3.1. Characterization of porous partially fluorinated graphene

The schematic diagram of the synthesis process is illustrated in Fig. 1. During the hydrothermal process with relatively high temperature, the hydrolysis of BF_4^- occurs gradually to BF_3OH^-, $BF_2(OH)_2^-$, and $BF(OH)_3^-$ and finally $B(OH)_4^-$ accompanied by the formation of HF [32]. This reaction mechanism is analogous to the fluorination process of UO_2 reported previously [33]. Additionally, boron atoms (2.0) which possess slightly lower electronegativity than carbon atoms (2.5) have strong affinity for fluorine atoms (4.0) [34]. Thus, carbon atoms of graphene lattice are more inclined to combine with free fluoride ions from hydrolysate HF.

Comparing the optical photographs of HRG (a) with 180-PFG (b) in Fig. S1, it is found that the dispersibility in the aqueous solution of the GO solution with sodium fluoroborate decreased after hydrothermal reaction. It is probably attributed to the reduced oxygen-containing functional groups and low surface energy of fluorinated graphene after the introduction of fluorine atoms [35]. Therefore, it can also be proved that fluorine atoms have been successfully introduced into graphene framework, which is consistent with the following XPS findings. The microstructures and morphologies of HRG and x-PFG (x = 120, 140, 160 180, 200) are further characterized by SEM as shown in Fig. 2a and b-f. In comparison with HRG, there are some visible pits on the surface of PFG, and interconnected PFG sheets form a hierarchical pore structure in favor of ions transmission and electron conduction. Thus, the abundant porous structure of partially fluorinated graphene demonstrates the existence of BF_4^- can influence the morphology of graphene during hydrothermal fluorination process, and provide a larger adsorption space for accessible electrolyte ions. Specifically, during the actual hydrothermal reaction, fluorination process probably plays an auxiliary role in favor of accelerating the reduction of graphene oxide, and then induce the continuous agglomeration and assembly of two-dimensional GO sheets resulting in the formation of the porous structure. It is also worth noting that 180-PFG owns denser pores than 140-PFG at the same magnification, resulting in the larger specific surface area (SSA). As displayed in a series of Fig. 2b-f of x-PFG, too high or low hydrothermal temperature was obviously not suitable for the formation of complete pore structure. From TEM results and the elemental mappings of PFG, it is indicated that fluorine atoms have been introduced into the graphene lattices and have homogeneous distributions on the surface of graphene.

X-ray photoelectron spectroscopic (XPS) spectra of x-PFG (x = 120, 140, 160 180, 200) and HRG are displayed in Fig. 3 and Fig. S2. The fluorine content and various chemical bonding components are primarily analyzed to elucidate the influence of hydrothermal temperature on fluorination process. As the full spectrum shown in Fig. 3a, both 180-PFG and 140-PFG with a signal of the distinct F 1s peak at around 686.0 eV prove introduction of fluorine atoms to carbon framework successfully, and 140-PFG that possesses a sharper peak demonstrates more fluorine atoms exists on it.

High resolution spectra analysis of C 1s is one of the most effective means to study the various types of C–F bonds for all the samples. Generally, the peak of C1s spectrum located at 284.8 eV is ascribed to sp^2 hybridized carbon atoms (C–C) without functionalization. The peaks centered at around 286.4 and 287.1 eV are corresponding to C=O and C–O groups, respectively [36]. In addition to the oxygen-containing functional groups attached to the carbon skeleton of graphene oxide, as-prepared partially fluorinated graphene obtained the characteristic peaks of C–F covalent bonds and C–F semi-ionic bonds. Thereinto, the peaks located at 285.8 eV (C*–CF) and 291.6 eV (C–F_2) are all assigned to covalent C–F bonds, and C*–CF represents one or two fluorine atoms are successfully grafted to the β position of the carbon atoms [16,37]. Besides, a vital and desired peak of semi-ionic C–F bonds can be observed near 288.8 eV. From Fig. S2a to S2c, the peak of C=O bonds disappears and the peak covalent C–F bonds (C–F_2 bonds) begin to emerge. When the hydrothermal temperature reaches up to 200 °C (Figure S2c), it is found that there are only C=C, C–O and

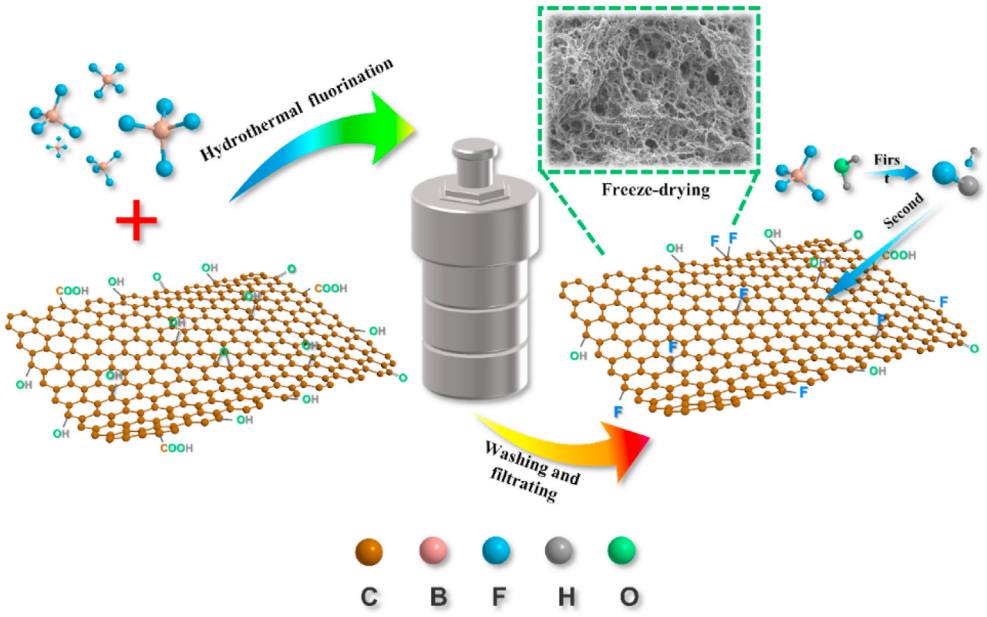

Fig. 1. Schematic illustration for the preparation of PFG.

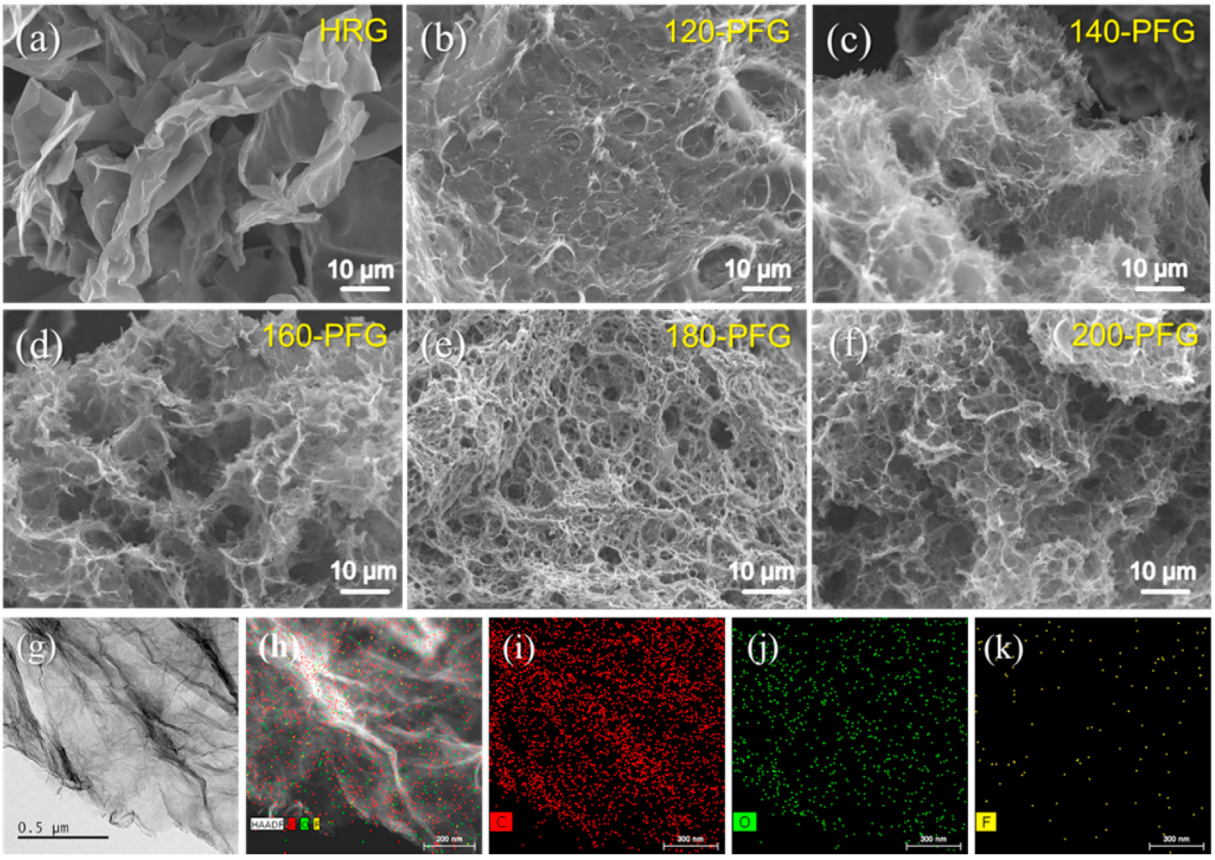

Fig. 2. (a–f) SEM images of HRG, x-PFG (x = 120, 140, 160 180, 200), (g–k) TEM images and corresponding elemental (C, O, F) mapping of PFG.

few C–F bonds, suggesting unsuitable circumstance (at 200 °C) for the formation of both covalent and semi-ionic C–F bonds.

In Table 1, the content of fluorine atoms and proportion of chemical bonds calculated from C 1s are recorded in detail. Both the fluorine content (1.05 at%) and the proportion of covalent C–F bonds in 140-PFG reach the highest among x-PFG (x = 120, 140, 160, 180, 200). It is analogous to fluorinating graphene using HF as the fluorine source, which follows the general law of the effect of reaction temperature on the formation of C–F bonds during the hydrothermal process [16]. In addition, it is worth noting that the

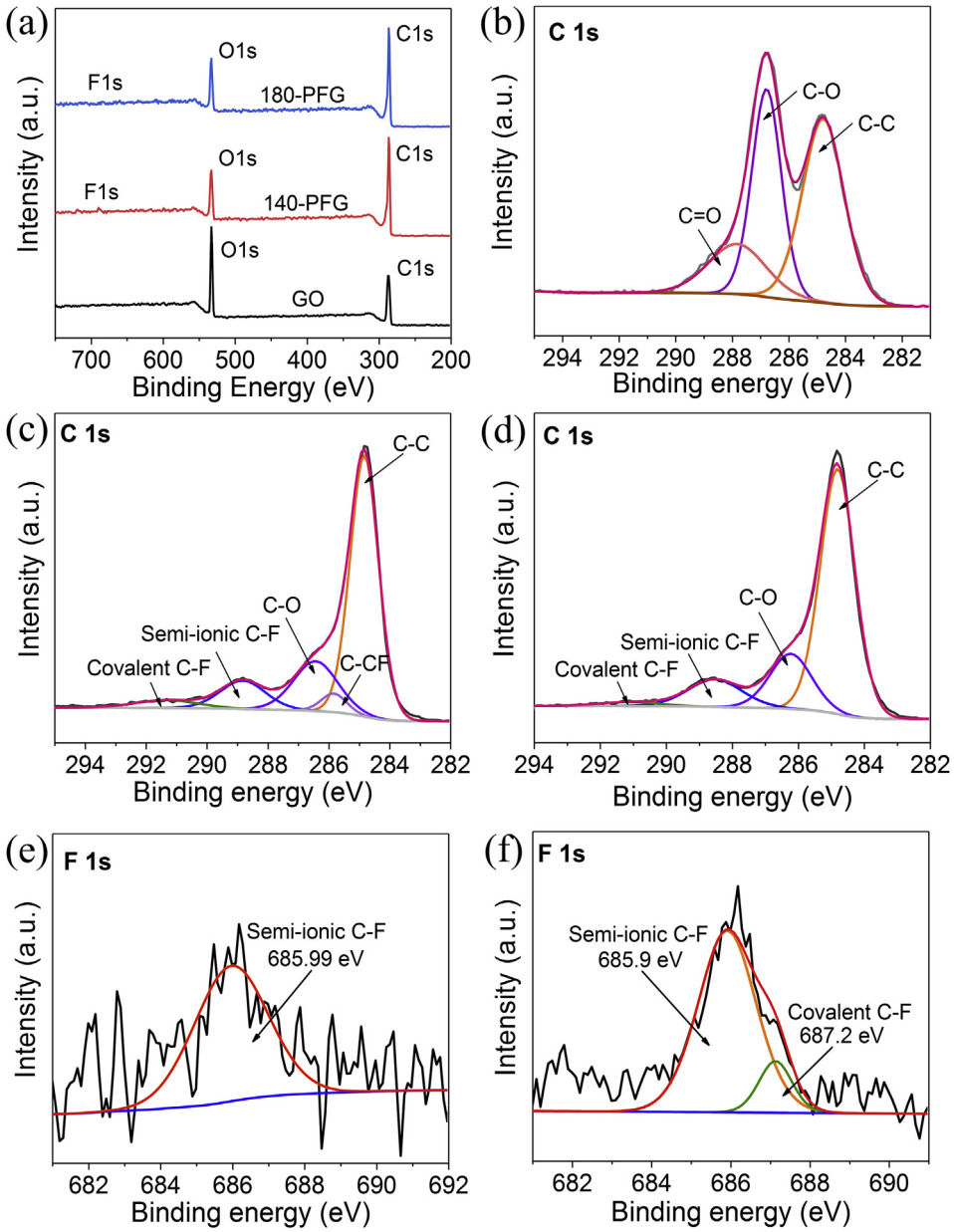

Fig. 3. (a) XPS survey spectra of the GO, 140-PFG and 180-PFG. (b–d) C1s spectra of GO, 140-PFG and 180-PFG. (e) F1s spectra of 180-PFG. (f) F1s spectra of 140-PFG.

Table 1
The fluorine content and proportion of different chemical bonds in C 1s.

Sample	C–C/%	covalent C–F/%	semi-ionic C–F/%	C–O/C=O/%	F/%
GO	45.9%	0	0	54.1%	0
120-PFG	68.5%	5.5%	4.1%	21.9%	0.32
140-PFG	62.5%	8.1%[a]	10.6%	18.8%	1.05[a]
160-PFG	65.4%	7.2%	11.1%	16.3%	0.60
180-PFG	67.6%	2.0%	12.2%[a]	18.2%	0.49
200-PFG	78.1%	0	3.1%	18.8%	0.47

F/% stands for the atomic percentages among C, O, F elements.
[a] Stands for the maximum value.

change law of semi-ionic C–F bonds differed from covalent C–F bonds. It is observed that the 180-PFG has the highest proportion of semi-ionic C–F bonds. On the basis of the previous studies on the formation of semi-ionic C–F bonds, it is speculated that when the hydrothermal temperature was lower than 180 °C, the fluorine ion concentration in the solution is relatively lower and it is gradually more inclined to form semi-ionic C–F bonds with the increase of temperature. However, when the hydrothermal temperature is higher than 180 °C, the relatively high fluorine ion content is not conducive to the formation of semi-ionic C–F bonds. Meanwhile, covalent C–F bonds cannot appear under a high temperature either [29]. The high resolution F1s signals of 140-PFG and 180-PFG are further assessed in Fig. 3e, f and the peaks of 140-PFG can be resolved into two peaks ascribing to covalent C–F bonds (687.2 eV) and semi-ionic C–F bonds (685.9 eV) [30]. As for 180-PFG, there is only one peak located at ~685.9 eV, meaning only semi-ionic C–F bonds have been obtained. These are consistent with the analysis results from high-resolution C 1s. To verify that no boron remains, the high-resolution B 1s peak is observed in Fig. S2d. No distinct peak is discovered. It is suggested that the boron compounds produced by the hydrolysis of BF_4^- during the hydrothermal fluorination process have been completely washed away by DI water. This

result can also be explained by the strong binding combination between B and F atoms.

Fourier transform infrared (FT-IR) spectroscopy was used further to investigate the major types of the chemical structure characteristics of 140-PFG, 180-PFG and GO, as presented in Fig. 4a. The broad feature peaks at around 3350 cm^{-1} are related to physisorbed water and phenol and hydroxyl groups in carboxylate moieties [32]. The typical absorption peaks and corresponding chemical bonds of GO includes ~1405 cm^{-1} (C–OH stretching), ~1625 cm^{-1} (C=C stretching), ~1728 cm^{-1} (C=O stretching) and ~1071 cm^{-1} (C–O stretching) [31]. After the hydrothermal fluorination reaction, these oxygen-containing functional groups have a downside, suggesting partial reduction of GO to some extent. To be specific, the peak intensity of the C=O chemical bonds of 140-PFG is the lowest, which implies the formation of C–F_2 by substituting oxygen atoms with fluorine atoms. With respect to the 140-PFG and 180-PFG samples, a new peak appears at ~1157 cm^{-1}, which can be ascribed to semi-ionic C–F bonds [33].

The structural changes were further investigated by means of the XRD patterns of 140-PFG, 180-PFG, HRG and GO, as shown in Fig. 4b. The diffraction peaks at $2\theta = 10.21°$ (d = 0.866 nm) are in accordance with the (001) planes of GO [38]. In addition, the peaks (002) of 140-PFG, 180-PFG and hydrothermally reduced graphene oxide are at around 25° corresponding to 24.50° (d = 0.363 nm), 25.40° (d = 0.350 nm) and 25.51° (d = 0.348 nm). The other diffraction peaks at about 43.0° are the (100) planes of 140-PFG, 180-PFG and HRG. These results demonstrate that pristine graphene oxide was reduced and the interlayer distance of graphene increased slightly after hydrothermally fluorination.

Raman spectra was analyzed on the microstructural changes (defects and disorder) of 180-PFG, HRG and GO, as shown in Fig. 4c. The D band and G band, which are main characteristic peaks of graphene materials, locate at around 1350 cm^{-1} and 1590 cm^{-1}, respectively. Generally, the intensity ratio of I_D/I_G values is utilized to illustrate the amount of defect [39]. According to the characterization results, a higher I_D/I_G value of 180-PFG (1.07) adequately demonstrated that fluorination reaction can increase the defects of pristine GO (0.91). Additionally, 180-PFG (1.07) has a nearly similar I_D/I_G value to HRG (1.02), and it can be attributed to the actual fluorination process where fluorine atoms replace the oxygen-containing functional groups linking to the sp^3 C sites [16]. Based on the analysis results of the above various characterization methods, it is evident that fluorine atoms have been introduced into carbon lattice and substantially impacted on the graphene framework. In term of XPS, FT-IR and Raman spectra analysis results, the possible reaction mechanism (Fig. 4d) of hydrothermal fluorination of GO in this work is consistent with the previous literature [40]. Three main oxygen-containing groups (hydroxyl, epoxy, carbonyl) provided reactive sites for fluorine atoms. The information of specific surface area (SSA) and the pore size distribution of as-prepared 180-PFG was obtained via N_2 adsorption-desorption measurements. As depicted in Fig. S3, the N_2 adsorption-desorption isotherm of 180-PFG confirms that it belongs to typical type IV isotherm characteristic with H_3-type hysteresis loop at relative pressure of 0.2–1.0, showing a large BET surface area of 170.5 $m^2\ g^{-1}$. Besides dominated microporous and macroporous structure of 180-PFG, a certain amount of mesoporous (2 nm–50 nm) is also observed clearly from pore size

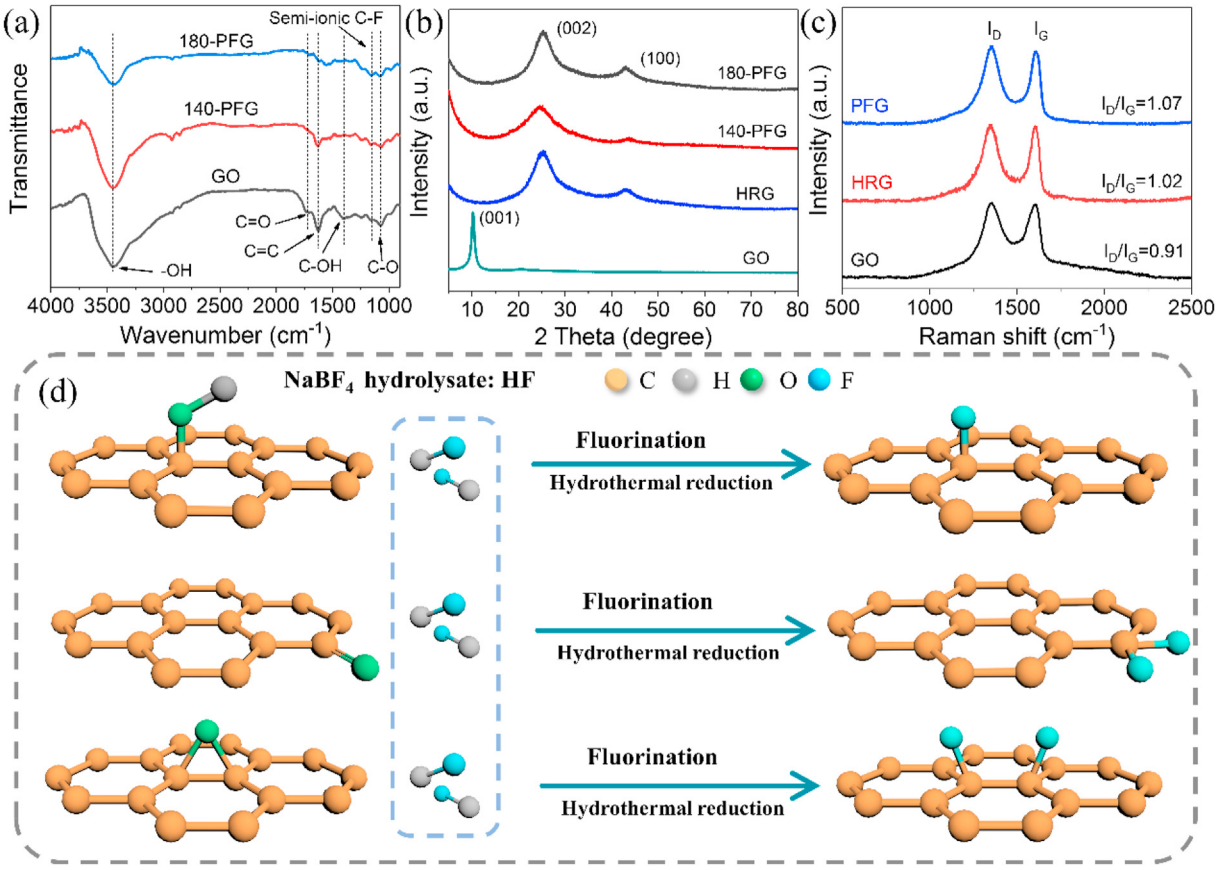

Fig. 4. (a) FT-IR. (b) XRD patterns of 140-PFG, 180-PFG, HRG and GO. (c) Raman spectra of PFG, HRG and GO. (d) Main fluorination reactions between oxygen-containing groups on the GO and HF obtained from $NaBF_4$ hydrolyzation.

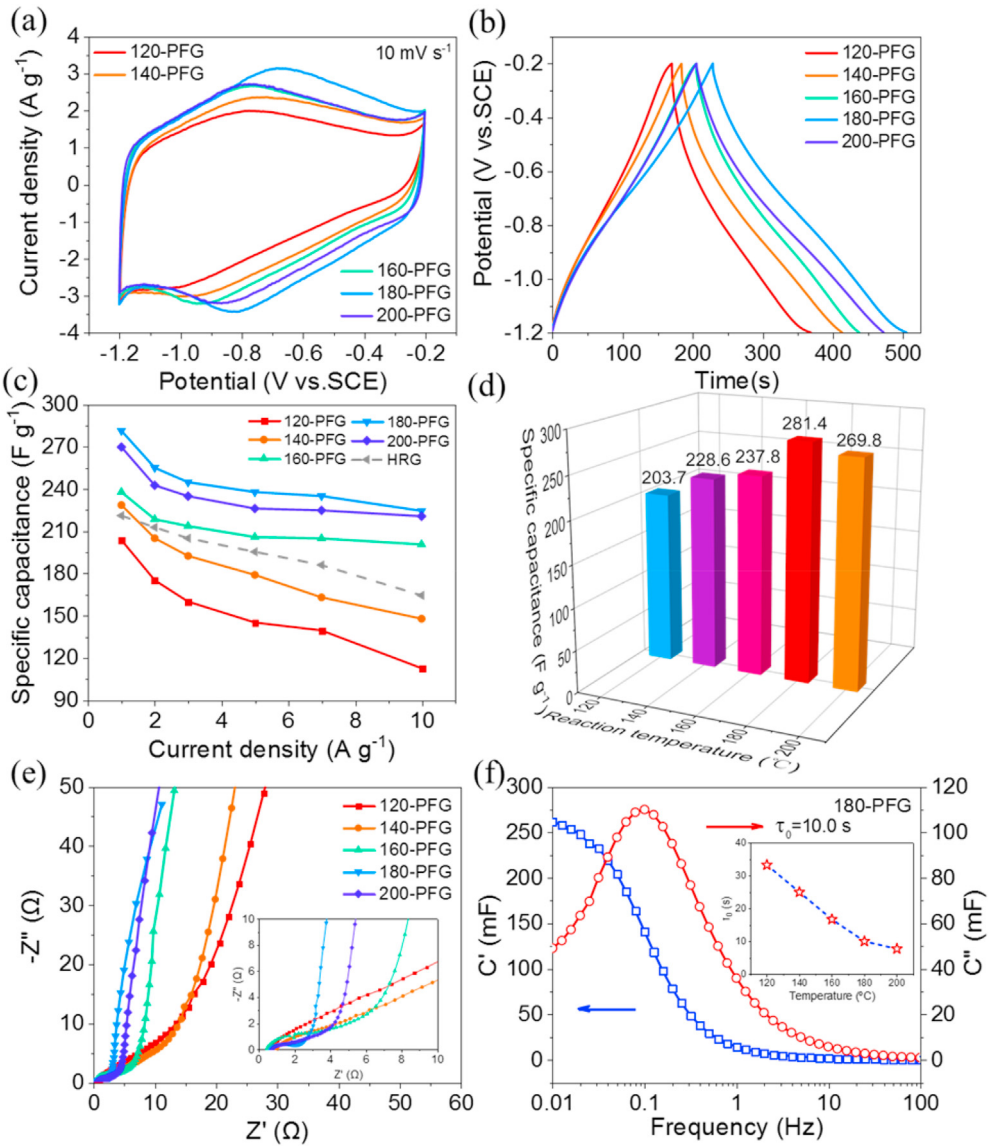

Fig. 5. Electrochemical performances of the x-PFG (x = 120, 140, 160, 180, 200). (a) CV curves at a scan rate of 10 mV s^{-1} in the three-electrode system. (b) GCD curves at a current density of 1 A g^{-1}. (c) Rate performances of x-PFGs and HRG. (d) The gravimetric specific capacitance values. (e) Nyquist plots. (f) Real and imaginary parts in Bode plots of 180-PFG (Inset: corresponding the time constant τ_0 vs. various temperatures plot.).

distribution (Fig. S3a, S3b). Actually, the existence of macroporous structure is benefit for electrolyte penetration, and mesoporous structure provides high specific surface area for storage charge. During hydrothermal reaction, the construction of abundant porous structure for partially fluorinated graphene is closely associated with the degree of fluorination modification.

3.2. Electrochemical performance

To systematically study the effect of hydrothermal temperature on the electrochemical performances, x-PFG (x = 120, 140, 160 180, 200) and HRG electrodes were measured by three-electrode configuration in 6 M KOH electrolyte firstly. The CV curves of 180-PFG and HRG electrodes at the scan rate of 10 m V s^{-1} are shown in Fig. S4a. The CV curves show near rectangular shapes, which is the typical feature of electric double-layer capacitance. The specific capacitance value (Fig. S4b) of graphene oxide, which is partially reduced by hydrothermal reaction, is only 221.0 F g^{-1} at 1 A g^{-1}180-PFG electrode with a larger area of CV curves illustrates the capacitance of materials is drastically improved owing to the extraneous fluorine atoms. Furthermore, the location of the faradaic redox peaks of PFGs approach −0.83 V (vs. SCE) in the cathodic scan and −0.67 V (vs. SCE) in the anodic scan. The growth of the pseudo-capacitance is inseparable from the introduction of C—F groups (covalent C—F bonds and semi-ionic C—F bonds) into partially reduced graphene oxide. The involved redox reaction process of fluorinated graphene in alkaline solution is probably that the introduction of fluorine atoms can endow the surrounding location of linked carbon with positively charged active sites and one-electron oxidation occurs along with hydroxide adsorption according to the previous report [41]. From the testing results shown in Fig. 5d, it is clearly indicated that 180-PFG obtains the highest specific capacitance among the PFG electrodes at various reaction temperature. As displayed in Fig. 5b, charge-discharge

curves of all the partially fluorinated graphene samples assumed the shape of nearly symmetrical triangle, illustrating the excellent reversible charge-discharge capacity. On the other hand, the specific capacitance of PFGs and HRG at different current densities ranging from 1 A g^{-1} to 10 A g^{-1} are shown in Fig. 5c. It is obvious that after fluorination, partially fluorinated graphene gained a better rate performance (80% of PFG» 74% of HRG), and the 180-PFG electrode is able to keep at a relatively reasonable level in the three-electrode system. The gravimetric specific capacitance values of x-PFG (x = 120, 140, 160, 180, 200) samples were calculated by the discharge time of GCD curves, corresponding to 203.7, 227.9, 232.1, 281.4, 269.8 F g^{-1}, respectively (Fig. 5d). Obviously, 180-PFG achieves the longest discharge time and largest integration area in the CV curve, indicating the possession of biggest specific capacitance (281.4 F g^{-1}).

In order to further evaluate the resistance performance of x-PFG samples, EIS was employed and the Nyquist plots were displayed in Fig. 5e. The inset of Fig. 5e presents the enlarged view of high frequency region. According to the equivalent circuit diagram shown in Fig. S8, the Nyquist plots were accurately fitted to calculate the corresponding solution resistance (R_s) and faradaic charge-transfer resistance (R_{ct}). In impedance Nyquist plots, the R_s consists of the intrinsic resistance of active material, ionic resistance of electrolyte and contact resistance between the current collector and electrode material [42]. The R_{ct} values calculated by the diameter of semicircle at the high-frequency region are associated with the pseudocapacitive behavior that occurs at the interface of electrode and electrolyte ions [43–45]. Besides, the plots of all the samples in the low frequency range exhibit a steep slope similar to a vertical, suggesting electrochemical process is dominated by electrical double layer capacitance. The fitted results in Table S1, x-PFG (x = 120, 140, 160, 180, 200) samples own relatively low R_s values (0.61, 0.95, 0.44, 0.63 and 0.70 Ω), which can contribute to the fast conduction of electrons and good wettability of electrode surface in the electrolyte. The 140-PFG owns the highest Rs (0.95 Ω) value and this can be attributed to reduced free electrons on the surface of graphene due to the formation of covalent C–F bonds and plentiful residual oxygen-containing functional groups as well as relatively poor wettability brought by covalent C–F bonds. It is worth mentioning that 180-PFG with the lowest R_{ct} value is able to easily store electric charge through faradaic reaction and thus it is reasonable that the highest specific capacitance of 180-PFG results from more pseudo-capacitance.

Complex Bode plots were further investigated to analyze the rate capability of a series of electrode materials. Fig. S6 show the real part (C′, mF) and the imaginary part (C″, mF) versus frequency (f, Hz) of x-PFG (x = 120, 140, 160, 180, 200) and HRG. In the plots of imaginary part of capacitance versus frequency, the relaxation time constant τ_0 can be obtained from the character frequency corresponding to the maximum C" ($f = 1/\tau_0$). Generally speaking, high power density supercapacitors are expected to be characterized by high character frequency and smaller τ_0, which is defined as the minimum time to discharge the whole energy with an efficiency greater than 50% [46,47]. First of all, the real part C′ change with frequency of 180-PFG and HRG are discussed in Fig. 5f and S4b. At the low frequency region (0.01–0.1 Hz), there is a gentler incline for 180-PFG, manifesting a fast pathway of the electrolyte ions. At the higher frequency region, sharp decrease of C′ value is attributed to the fact that only the near surface of the pores can be accessed by the electrolyte ions [48]. The 180-PFG has a character frequency of 0.10 Hz corresponding to the time constant of 10.0 s, which is better than 0.03 Hz and 33.3 s for the HRG, suggesting a faster charge-discharge characteristic response after fluorination. Among these five PFG electrodes from the C′ vs. frequency plot in Fig. S6a, the 180-PFG with the highest C′ value demonstrates its optimal storage property. In Figure S6c, it can be seen that the character frequency of x-PFG (x = 120, 140, 160, 180, 200) are 0.03, 0.04, 0.06, 0.10, 0.13 Hz, corresponding to the time constant τ_0 of 33.3, 25.0, 16.7, 10, 7.7 s, respectively. The increased capacitance of 180-PFG results in a shift to a lower frequency comparing with 200-PFG and both of frequency values of them were kept at a reasonable range. To sum up, 180-PFG in bode plots is proved to have relatively outstanding performance likewise and 180 °C is the optimal temperature for fabricating this electrode material.

In consideration of the best electrochemical performance of 180-FPG sample, it was selected as the electrode materials to assemble symmetrical coin cells. All the two-electrode system measurements were carried out in 6 M KOH solution as the electrolyte with the stable operating potential window (1.0 V). As shown in Fig. 6a, all the CV curves assume quasi-rectangular shapes without any apparent redox peaks, which are different from three-electrodes testing results. Meanwhile, the ideal symmetrical triangle presents through GCD curves is ascribed to the good reversibility of this device (Fig. S7). Voltage drops at the beginning of the discharge can be barely found in the GCD curves, indicating that the device has fast current/voltage response with a low resistance. As for the rate performance, the gravimetric specific capacitance values calculated from GCD curves at various current densities are shown in Fig. 6b. The specific capacitance of 180-PFG tends to decrease with the increase of the current density. The highest gravimetric specific capacitance of 269.7 F g^{-1} is reached at the current density of 1 A g^{-1}, but the 180-PFG still achieves the specific capacitance of 240.8 F g^{-1} even at a higher current density of 20 A g^{-1}, illustrating outstanding capacitance retention (89%). The result from Nyquist plots (Fig. S6d) proves that there is very low resistance for electrolyte ions delivery and electron transportation in assembled symmetrical coin cells. Especially, the energy density of 9.4 Wh kg^{-1} is obtained with corresponding power density 250.0 W kg^{-1} at current density of 1 A g^{-1}. While the current density is increased to 20 A g^{-1}, the maximum power density of 5.02 kW kg^{-1} is obtained and the corresponding energy density was 8.36 Wh kg^{-1}. Notably, capacitive performance of our symmetric supercapacitors is higher than those of fluorinated graphene fabricated via traditional hydrothermal approach with HF and some nitrogen-doped carbon materials such as FGH and N-MGHs [49]. The cycle stability of this symmetric supercapacitor device was measured on the CT3001K testing system, and 180-PFG electrode retained about 92.3% capacitance after 5000 cycles at the current density of 4 A g^{-1} (Fig. 6c). Ragone plots displayed in Fig. 6d show the outstanding energy density and power density of as-fabricated PFG compared to other single-element doping graphene and some details are listed in Table S2. Electrochemical performances in different aspects have amply demonstrated that as-prepared porous partially fluorinated graphene is a potential electrode material for supercapacitors, especially due to its rather high specific capacitance and splendid capacity retention rate.

In consideration of overall experimental results above, the superior capacitive performances of PFG may be ascribed to the following reasons: Firstly, the partially fluorinated graphene with the semi-ionic C–F bonds was endowed with an enhanced conductor of electricity, and good wettability between electrode and electrolyte was actually attributed to macro-porous structure formed under the participation of BF_4^-; secondly, after fluorination, the stability of semi-ionic C–F bonds enhance the rate capability of electrodes; thirdly, the as-fabricated partially fluorinated graphene formed abundant porous structures in favor of electron delivering in the graphene networks and ion fast transfer pathway in the electrolyte.

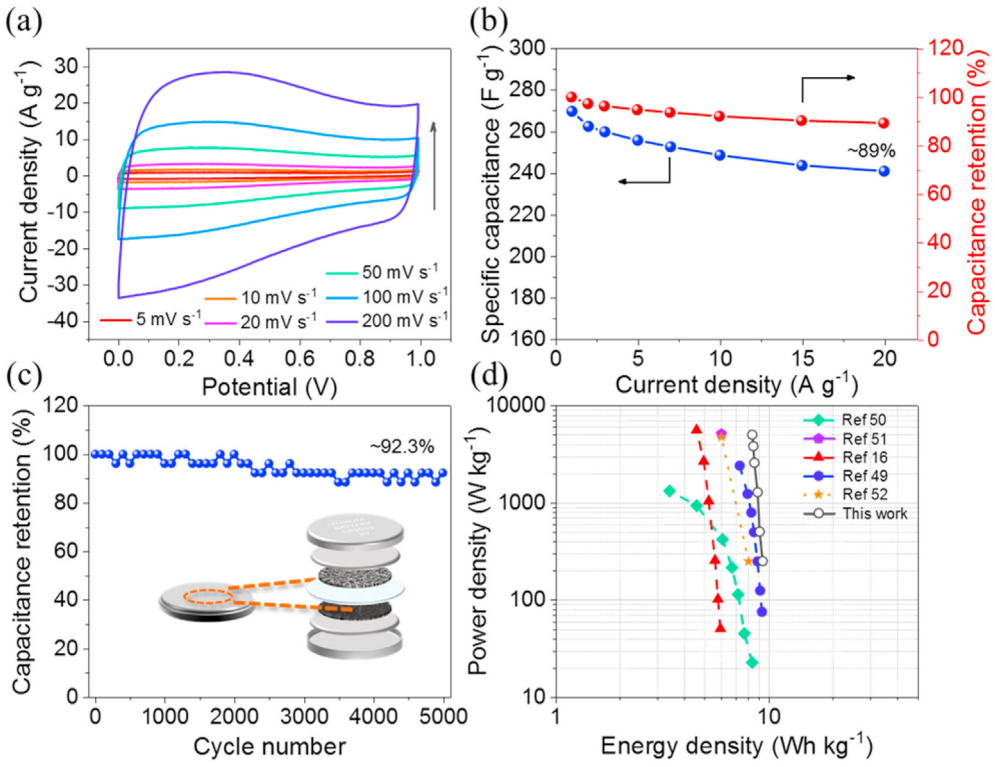

Fig. 6. (a) CV curves of the assembled symmetric supercapacitors at the scan rate from 5 mV s^{-1} to 200 mV^{-1}. (b) Specific capacitance and the corresponding capacitance retention at different current densities. (c) The long-term cycling stability (92.3%) of the symmetric supercapacitors for 180-PFG at 4 A g^{-1}. (d) Ragone plots of the symmetric supercapacitor of 180-PFG in comparison with previous relevant reports [16,49–52].

4. Conclusions

In summary, we fabricated porous partially fluorinated graphene via a facile and high security one-pot hydrothermal method for enhanced high-performance symmetric supercapacitors. Unlike direct exposure of carbon-based materials to solutions containing large amounts of fluoride ions, this work utilized the stepwise hydrolysate of weakly coordinating anion BF_4^- as the fluorine source to realize the fluorination of GO at various temperatures. The sodium fluoborite ($NaBF_4$) is only subject to hydrolysis reaction at relatively high temperature, which not only ensures the safety of the experimental process for operators, but also accomplishes the modification for graphene electrode materials with better electrochemical performances than traditional fluorinating agent. The results demonstrated that appropriate hydrothermal temperature enabled as-fabricated 180-PFG to have enough semi-ionic C–F bonds nearly without covalent C–F bonds, achieving the optimum electrochemical performances, and a reasonable speculation was proposed on the change law of the proportion of semi-ionic and covalent C–F bonds with the variation of the reaction temperature. Remarkably, symmetric supercapacitors assembled by 180-PFG exhibited an exceptional specific capacitance of 269.1 F g^{-1} at 1 A g^{-1} with outstanding rate performance of 89.3% capacity retention (20 A g^{-1}) and high energy density of 9.4 Wh kg^{-1} at power density of 250.0 W kg^{-1}. An enhanced electrochemical performance for SCs, especially gravimetric specific capacitive and rate performances, underpins its value for practical application. All these relevant researches are designed to advance the development of partially fluorinated graphene in the field of the supercapacitors. Green and secure synthesis for fluorinated carbon-based materials is one of crucial research direction in the future.

Declaration of competing interest

The authors declare that they have no known competing financial interests or personal relationships that could have appeared to influence the work reported in this paper.

Acknowledgements

This work was supported by National Natural Science Foundation of China (21905304), Natural Science Foundation of Shandong Province (ZX20210028) and the Fundamental Research Funds for the Central Universities (19CX05001A).

Appendix A. Supplementary data

Supplementary data to this article can be found online at https://doi.org/10.1016/j.jmat.2021.04.012.

References

[1] Shao Y, El-Kady MF, Sun J, Li Y, Zhang Q, Zhu M, Wang H, Dunn B, Kaner RB. Chem Rev 2018;118:9233–80. https://doi.org/10.1021/acs.chemrev.8b00252.
[2] Chen XL, Paul R, Dai LM. Natl Sci Rev 2017;4:453–89. https://doi.org/10.1093/nsr/nwx009.
[3] Noori A, El-Kady MF, Rahmanifar MS, Kaner RB, Mousavi MF. Chem Soc Rev 2019;48:1272–341. https://doi.org/10.1039/c8cs00581h.
[4] Zang XB, Wang JL, Qin YJ, Wang T, He CP, Shao QG, Zhu HW, Cao N. Nano-Micro Lett 2020;12:24. https://doi.org/10.1007/s40820-020-0415-5.
[5] Yan J, Wang Q, Wei T, Fan ZJ. Adv Energy Mater 2014;4. https://doi.org/10.1002/aenm.201300816.
[6] Liao Q, Jin S, Wang C. Journal of Materiomics 2016;2:291–308. https://doi.org/10.1016/j.jmat.2016.09.002.
[7] Song H, Su J, Wang C. Adv Mater 2021;33:e2006141. https://doi.org/10.1002/adma.202006141.
[8] Song H, Su J, Wang C. Adv Energy Mater 2021;11:2003685. https://doi.org/

10.1002/aenm.202003685.
[9] Jin YN, Meng YN, Fan W, Lu HY, Liu TX, Wu SX. Electrochim Acta 2019;318:865–74. https://doi.org/10.1016/j.electacta.2019.06.107.
[10] Bose S, Kuila T, Mishra AK, Rajasekar R, Kim NH, Lee JH. J Mater Chem 2012;22:767–84. https://doi.org/10.1039/c1jm14468e.
[11] Jiang L, Fan Z. Nanoscale 2014;6:1922–45. https://doi.org/10.1039/c3nr04555b.
[12] Gao Y, Wang L, Li Z, Zhang Y, Xing B, Zhang C, Zhou A. Journal of Advanced Ceramics 2015;4:130–4. https://doi.org/10.1007/s40145-015-0143-3.
[13] Sun H, Liu H, Hou Z, Zhou R, Liu X, Wang J-G. Chem Eng J 2020;387. https://doi.org/10.1016/j.cej.2020.124204.
[14] Zhou J, Lian J, Hou L, Zhang J, Gou H, Xia M, Zhao Y, Strobel TA, Tao L, Gao F. Nat Commun 2015;6:8503. https://doi.org/10.1038/ncomms9503.
[15] Zhou HH, Peng YT, Wu HB, Sun F, Yu H, Liu F, Xu QJ, Lu YF. Nanomater Energy 2016;21:80–9. https://doi.org/10.1016/j.nanoen.2015.12.016.
[16] An HR, Li Y, Long P, Gao Y, Qin CQ, Cao C, Feng YY, Feng W. J Power Sources 2016;312:146–55. https://doi.org/10.1016/j.jpowsour.2016.02.057.
[17] He JJ, Wang N, Yang Z, Shen XY, Wang K, Huang CS, Yi YP, Tu ZY, Li YL. Energy Environ Sci 2018;11:2893–903. https://doi.org/10.1039/c8ee01642a.
[18] Lee YS, Cho TH, Lee BK, Rho JS, Lee YH. J Fluor Chem 2003;120:99–104. https://doi.org/10.1016/S0022-1139(02)00316-0.
[19] Cheng L, Jandhyala S, Mordi G, Lucero AT, Huang J, Azcatl A, Addou R, Wallace RM, Colombo L, Kim J. ACS Appl Mater Interfaces 2016;8:5002–8. https://doi.org/10.1021/acsami.5b11701.
[20] Fan K, Fu J, Liu X, Liu Y, Lai W, Liu X, Wang X. Chem Sci 2019;10:5546–55. https://doi.org/10.1039/c9sc00975b.
[21] Robinson JT, Burgess JS, Junkermeier CE, Badescu SC, Reinecke TL, Perkins FK, Zalalutdniov MK, Baldwin JW, Culbertson JC, Sheehan PE, Snow ES. Nano Lett 2010;10:3001–5. https://doi.org/10.1021/nl101437p.
[22] Vizintin A, Lozinšek M, Chellappan RK, Foix D, Krajnc A, Mali G, Drazic G, Genorio B, Dedryvère R, Dominko R. Chem Mater 2015;27:7070–81. https://doi.org/10.1021/acs.chemmater.5b02906.
[23] Saha S, Samanta P, Murmu NC, Banerjee A, Ganesh RS, Inokawa H, Kuila T. Chem Eng J 2018;339:334–45. https://doi.org/10.1016/j.cej.2018.01.141.
[24] Poh HL, Sofer Z, Klimova K, Pumera M. J Mater Chem C 2014;2:5198–207. https://doi.org/10.1039/c4tc00395k.
[25] Abdelkader-Fernández VK, Morales-Lara F, Melguizo M, García-Gallarín C, López-Garzón R, Godino-Salido ML, López-Garzón FJ, Domingo-García M, Pérez-Mendoza MJ. Appl Surf Sci 2015;357:1410–8. https://doi.org/10.1016/j.apsusc.2015.09.262.
[26] Zhao FG, Zhao G, Liu XH, Ge CW, Wang JT, Li BL, Wang QG, Li WS, Chen QY. J Mater Chem 2014;2:8782–9. https://doi.org/10.1039/c4ta00847b.
[27] Zhou S, Sherpa SD, Hess DW, Bongiorno A. J Phys Chem C 2014;118:26402–8. https://doi.org/10.1021/jp508965q.
[28] Peng W, Li H, Song S. ACS Appl Mater Interfaces 2017;9:5204–12. https://doi.org/10.1021/acsami.6b11316.
[29] Walter AL, Jeon K-J, Bostwick A, Speck F, Ostler M, Seyller T, Moreschini L, Kim YS, Chang YJ, Horn K, Rotenberg E. Appl Phys Lett 2011;98:184102. https://doi.org/10.1063/1.3586256.
[30] Laheäär A, Przygocki P, Abbas Q, Béguin F. Electrochem Commun 2015;60:21–5. https://doi.org/10.1016/j.elecom.2015.07.022.
[31] Chen YJ, Liu ZE, Sun L, Lu ZW, Zhuo KL. J Power Sources 2018;390:215–23. https://doi.org/10.1016/j.jpowsour.2018.04.057.
[32] Koji S, Yukihiro Y, Hideyuki F, Akio S. J Mol Liq 2016;219:493–6. https://doi.org/10.1016/j.molliq.2016.03.036.
[33] Florian J, Pardis S, Xavier T, Mehdi A, Bertrand M, Lorenzo SP, Jean-Francois P, Philippe M, Christophe V. Dalton Trans 2020;49:274–8. https://doi.org/10.1039/c9dt04327f.
[34] Feng W, Long P, Feng Y, Li Y. Adv Sci 2016;3:1500413. https://doi.org/10.1002/advs.201500413.
[35] Jayaramulu K, Datta KKR, Rosler C, Petr M, Otyepka M, Zboril R, Fischer RA. Angew Chem Int Ed 2016;55:1178–82. https://doi.org/10.1002/anie.201507692.
[36] Wang Y, Song Y, Xia Y. Chem Soc Rev 2016;45:5925–50. https://doi.org/10.1039/c5cs00580a.
[37] Vermisoglou EC, Jakubec P, Bakandritsos A, Pykal M, Talande S, Kupka V, Zboril R, Otyepka M. Chem Mater 2019;31:4698–709. https://doi.org/10.1021/acs.chemmater.9b00655.
[38] Zhao SH, Xu WW, Yang ZB, Zhang XY, Zhang QY. Electrochim Acta 2020;331. https://doi.org/10.1016/j.electacta.2019.135265. 26146-26146.
[39] Domga Karnan M, Oladoyinbo F, Noumi GB, Tchatchueng JB, Sieliechi MJ, Sathish M, Pattanayak DK. Electrochim Acta 2020;341:14. https://doi.org/10.1016/j.electacta.2020.135999.
[40] Wang ZF, Wang JQ, Li ZP, Gong PW, Liu XH, Zhang LB, Ren JF, Wang HG, Yang SR. Carbon 2012;50:5403–10. https://doi.org/10.1016/j.carbon.2012.07.026.
[41] Kim J, Fukushima T, Zhou R, Murakoshi K. Materials 2019;12. https://doi.org/10.3390/ma12020211.
[42] Chen JJ, Huang Y, Li C, Chen XF, Zhang X. Appl Surf Sci 2016;360:534–9. https://doi.org/10.1016/j.apsusc.2015.10.187.
[43] Zhang Y, Wen GW, Fan S, Ma WH, Li SH, Wu T, Yu ZC, Zhao BR. Electrochim Acta 2019;313:59–69. https://doi.org/10.1016/j.electacta.2019.05.021.
[44] Zhang JL, Jiang M, Xing LB, Qin K, Liu TZ, Zhou J, Si WJ, Cui HY, Zhuo SP. Chin J Chem 2016;34:46–52. https://doi.org/10.1002/cjoc.201500656.
[45] Zhang L, Zhang F, Yang X, Long GK, Wu YP, Zhang TF, Leng K, Huang Y, Ma YF, Yu A, Chen YS. Sci Rep 2013;3:9. https://doi.org/10.1038/srep01408.
[46] Zhi MJ, Manivannan A, Meng FK, Wu NQ. J Power Sources 2012;208:345–53. https://doi.org/10.1016/j.jpowsour.2012.02.048.
[47] Ali GAM, Wahba OAG, Hassan AM, Fouad OA, Chong KF. Ceram Int 2015;41:8230–4. https://doi.org/10.1016/j.ceramint.2015.02.100.
[48] A M, A P. ACS Omega 2017;2:8039–50. https://doi.org/10.1021/acsomega.7b01275.
[49] Zhang Y, Wen GW, Gao P, Bi SF, Tang XF, Wang D. Electrochim Acta 2016;221:167–76. https://doi.org/10.1016/j.electacta.2016.10.115.
[50] Fan XM, Yu C, Yang J, Ling Z, Qiu JS. Carbon 2014;70:130–41. https://doi.org/10.1016/j.carbon.2013.12.081.
[51] Mohanraju K, Youngkwang K, Yung-Eun S, Joong KO. J Mater Chem 2018;6:7522–31. https://doi.org/10.1039/c8ta00028j.
[52] Na W, Jun J, Park JW, Lee G, Jang J. J Mater Chem 2017;5:17379–87. https://doi.org/10.1039/c7ta04406b.

Dr. Ning Cao is currently an Associate Professor at China University of Petroleum (East China). He received his Ph.D. in the School of Materials Science and Engineering, Shandong University, China, and received his B.S. degree (2004) and M. S. degree (2007) from the School of Materials Science and Engineering, Shandong University, China. His research interests focus on new carbon based nanostructure for energy and environment application.

Teng Wang received his Master degree from the School of China University of Petroleum (East China), Qingdao 266 580, PR China in 2021. He received a national scholarship during his study.His research interests mainly focus on the preparation of transition metal-based composite, functional graphene such as fluorinated graphene and sulfonate graphene and their application in supercapacitors and second-battery.

Dr. Xiaobei Zang is currently an Assistant Professor at China University of Petroleum (East China). She received her Ph.D. in the school of Materials Science and Engineering, Tsinghua University, China, and received her B.S. degree (2007) and M.S. degree (2010) from the College of Mechanical and Electronic Engineering, China University of Petroleum (East China). Her research interests focus on nano-carbon materilas-base electrode materials for flexible energy storage devices.